J. Fluid Mech. (2000), *vol.* 411, *pp.* 187–211. Printed in the United Kingdom

Turbulence cascade and dynamical exchange between spatial scales

By CYRILLE HONORÉ AND DOMINIQUE GRÉSILLON

Laboratoire de Physique des Milieux Ionisés (UMR 7648 du CNRS), École Polytechnique, F-91128 Palaiseau cedex, France

(Received 12 January 1998 and in revised form 5 January 2000)

The information exchange dynamics between different spatial scales of a turbulent field is experimentally investigated, with particular reference to the energy cascade process. This is done by use of the collective light scattering (CLS) diagnostic, a new optical setting tuned for the observation of atomic number density fluctuations at macroscopic scales. A two-channel scattering device is described that provides simultaneously the fluctuations at two different spatial scales. The turbulent system is an axisymmetric air jet. With this system, time correlations between signal amplitudes for two different scales show a characteristic time width. This time does not depend on the observed scales: it is close to the turbulence production time. Nevertheless, signal amplitude autocorrelation shows a shorter characteristic time. The autocorrelation time scaling law behaves almost like the eddy turnover time from Kolmogorov theory.

1. Introduction

1.1. *Collective light scattering: a lengthscale-sensitive flow diagnostic*

An accepted concept of the Richardson phenomenological turbulence approach is that large vortices drive smaller ones (see e.g. Frisch 1995). More specifically, Kolmogorov considered vortex amplitudes for a given scale as the space Fourier transform of the velocity field at the corresponding wavelength. He predicted a universal behaviour of these amplitudes as a function of the scale in the so-called 'inertial range'. In this scale range, energy is said to be transferred from large to small wavelengths. It is then natural to investigate with experiments whether and how this energy motion can be characterized.

Up to now, spatial spectrum observations have relied mostly on temporal sequences from point diagnostics such as hot wires. This provides time–frequency spectra, but these have been converted into wavevector spectra on the assumption of a large mean flow velocity whereby a wavevector is associated with a Doppler frequency. This is not satisfactory however, since not only is the large mean flow velocity assumption not always accurate, but also a conversion from one-dimensional frequency space is unable to recover the three-dimensional k-space. Moreover it is not clear how an energy transfer between different spatial scales can be embedded into information from a single point. Multiwire systems have been developed by J.-P. Bonnet, from which different wavevector components can be obtained. However these are intrusive devices, and appropriate wavevector resolution requires a large number of wires and a large amount of data.

There exists however a particular non-intrusive diagnostic that provides, as a single

time sequence, an accurate space Fourier transform at a given wavevector $\boldsymbol{k}$. It is collective light scattering (CLS), a device that is sensitive to the macroscopic space modulation of the refraction index. In homogeneous gas turbulence, the optical index is locally proportional to the gas number density and the CLS signal provides an instant number-density-space Fourier transform.

The gas number density k-spectrum in simple turbulent flows has been observed (Stern & Grésillon 1983) to be very close to the expected Kolmogorov behaviour, i.e. with the one-dimensional inertial-range-scale exponent. Thus although CLS provides the number density turbulent field instead of the velocity field, its signal behaves according to the expected turbulence universality.

1.2. *Turbulence dynamics investigations*

Nonlinear fluid dynamics is frequently investigated in Fourier space (Orszag 1977). In such a space, the nonlinearities are seen as coupling between Fourier modes of different wavevectors. If one intends to experimentally observe these couplings, it is more accurate to use several simultaneous CLS diagnostics, each of them being tuned to a different k-vector and used as a marker of the dynamics of this scale (see Grésillon & Mohamed-Benkadda 1998). Three different CLS channels were selected such that their scattering wavevectors satisfy $\boldsymbol{k}_1 + \boldsymbol{k}_2 = \boldsymbol{k}_3$. These signals were simultaneously recorded, and the bispectrum was calculated as the mean value of their product (the third-order statistical moment). For the simple cases of single mode instability, a significant coupling was found, but for cases of fully developed turbulence, the bispectrum values were only marginally significant.

Simple second-order linear statistics between two CLS signals is inappropriate for detecting a nonlinear coupling: since the characteristic signal frequency depends on the spatial scale as $\boldsymbol{k} \cdot \bar{\boldsymbol{v}}_o$ (a product of the wavevector times the flow velocity) the characteristic frequencies of two different scales are different and the signal correlation averages to zero. To avoid this frequency mismatch effect, one may either correlate the amplitude of the complex Fourier transforms (instead of correlating a single component, real or imaginary) at two different scales, or use a nonlinear comparison, such as the 'mutual information', between two signal components. The former method will be reported in this paper. The latter is based on the signal entropy method.

This was performed on two CLS signals (Grésillon, Cabrit & Iwana 1993). Using 'mutual information', the real parts of the CLS signal at different scales were found to be significantly dependent, over large time delays. A weak time asymmetry of the mutual information was observed between signal at different scales. But the statistical significance and the scattering lengthscale exploration were limited by data acquisition and optical setup performance.

1.3. *Extended lengthscale relation study*

The aim of this work is to extend these previous studies to experimentally establish the relation between the signal at different scales and try to understand the nature of this relation. As explained above, the phase and modulus analysis of the scattering complex signal is more relevant than a real and imaginary parts analysis since the scale information is mostly included in CLS signal modulus, while the signal phase essentially contains, through the Doppler effect, velocity information that is not specific to the observed scale.

In this paper, both mutual information and cross-correlation between collective scattering signals obtained from a purpose-built optical diagnostic device at two different scales will be investigated, especially the cross-correlation, which is easier

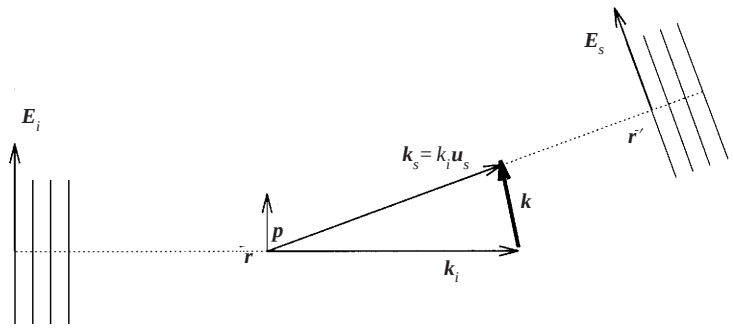

FIGURE 1. Light scattering by a molecular gas. An incident electric field $\boldsymbol{E}_i(\boldsymbol{k}_i, \omega_i)$ from a laser lights the gas flow (number density: $n(\boldsymbol{r}, t)$). A detector (direction $\boldsymbol{r}'$, scattering angle θ) collects the electric field $\boldsymbol{E}_s(k_i\boldsymbol{u}_s, \omega_i)$ scattered from the incident beam by gas molecules. The scattering wavevector is defined as the difference between scattered and incident wavevector $\boldsymbol{k} = k_i\boldsymbol{u}_s - \boldsymbol{k}_i$.

to compute and interpret. A specific CLS device with two independent channels has been built for this experiment and set in a simple gas turbulent flow. It has been used to study time crosscorrelation between different lengthscales within the inertial range in this gas turbulence. The optical sensitivity recording depth was increased to reach a large signal to noise ratio so as not only to observe a significant crosscorrelation but also to investigate at which level a time asymmetry or causality may or not exist between different lengthscales of the inertial range.

The aspects of the CLS technique relevant to this investigation will be presented in the next section, emphasizing the real and imaginary components of the signal, its modulus and the phase Doppler shift contribution. The third section describes the experimental assembly: the CLS device that can observe two different simultaneous scattered signals and the air jet turbulent device. The last section is devoted to the experimental results and shows the time crosscorrelation obtained between signal moduli at different scales. The dependence on the main experimental parameters is analysed and their reduction to a unique parameter is shown. The time crosscorrelation behaviour is discussed.

2. Collective light scattering and scale information

The basic CLS setup (Grésillon *et al.* 1982) is sketched in figure 1. A plane electromagnetic wave, e.g. from a laser source, lights a transparent medium. Spatial modulation of the dielectric constant produces a partial diffraction that can be detected as secondary waves, propagating in oblique directions such as along $\boldsymbol{u}_s$.

2.1. *Physical principle*

The observation principle is based on elastic light scattering (see Jackson 1975). The first fluid laser scattering observations were obtained by Cummins, Knable & Yeh (1964) and Yeh & Cummins (1964) for a colloidal suspension. Their method was extended to more common fluids, like water or air flows by de Gennes (1966), Frisch (1967) and Benedek (1964). J.-C. Lelièvre (Lelièvre & Picard 1980) obtained the first observations of a turbulent air jet.

Unlike laser velocimetry which uses scattering from small particles, CLS uses the gas molecules themselves as scatterers. The scattered E-field amplitude is shown to be proportional to the spatial Fourier transform of the gas atomic number density along the scattering wavevector (Cummins & Swinney 1970). Since the selected wavelength

scale is much larger than the mean free path, the phase shift due to molecular motion can be neglected: molecules are seen as frozen in the fluid. Changes in the scattered E-field phase are due to the macroscopic motion.

Molecular scattering

The E-field amplitude and phase can be characterized as follows. An incident monochromatic electromagnetic field of pulsation ω_i, wavevector $\boldsymbol{k}_i$, and amplitude $\boldsymbol{E}_{io}$ propagates through the gas:

$$\boldsymbol{E}_i(\boldsymbol{r}, t) = \boldsymbol{E}_{io} \mathrm{e}^{\mathrm{i}(\boldsymbol{k}_i \cdot \boldsymbol{r} - \omega_i t)}. \tag{2.1}$$

Each lit molecule (position: $\boldsymbol{r}_j$) reacts as an induced electric dipole of amplitude proportional to the incident electric field. The molecule polarizability is α_j, and the induced electric dipole moment is

$$\boldsymbol{p}_j(t) = \varepsilon_o \alpha_j \boldsymbol{E}_i(\boldsymbol{r}_j, t). \tag{2.2}$$

This dipole radiates a spherical electric field. This scattered electric field is detected far enough from the observation volume for the far-field approximation to be valid. The scattered electric field near to the detector can be approximated as a plane monochromatic wave. Since the scattering is elastic, the wavenumber is the same as the incident one. Its direction $\boldsymbol{u}_s$ is determined by the detector position:

$$\boldsymbol{k}_s = k_i \boldsymbol{u}_s. \tag{2.3}$$

When the dipole radiated field is expressed in term of the incident field from equations (2.1) and (2.2), the scattered electric field is obtained as

$$\boldsymbol{E}_{sj}(\boldsymbol{r}', t) = \frac{\pi \alpha_j}{N^2 \lambda_i^2} \frac{\mathrm{e}^{\mathrm{i}k_s r'}}{r'} \boldsymbol{u}_s \wedge [\boldsymbol{u}_s \wedge \boldsymbol{E}_{io}] \mathrm{e}^{-\mathrm{i}\omega_i t} \mathrm{e}^{\mathrm{i}(\boldsymbol{k}_i - \boldsymbol{k}_s) \cdot \boldsymbol{r}_j} \tag{2.4}$$

where N is the medium optical mean index and λ_i the vacuum wavelength. The last factor is the spatial phase factor. Its modulation is defined by the 'scattering' wavevector $\boldsymbol{k}$:

$$\boldsymbol{k} = \boldsymbol{k}_s - \boldsymbol{k}_i. \tag{2.5}$$

This scattering wavevector is shown in figure 1.

Scattering from non-uniform fluid

The total electric field that is received by the detector is a sum of scattered fields from each molecule inside the observation volume V. The volume V is defined as the intersection between the incident laser beam and the detector antenna beam (Holzhauer & Massig 1978):

$$\boldsymbol{E}_s(\boldsymbol{r}', t) = \frac{\pi}{N^2 \lambda_i^2} \frac{\mathrm{e}^{\mathrm{i}k_s r'}}{r'} \mathrm{e}^{-\mathrm{i}\omega_i t} \sum_j \alpha_j \boldsymbol{u}_s \wedge [\boldsymbol{u}_s \wedge \boldsymbol{E}_{io}] \mathrm{e}^{-\mathrm{i}\boldsymbol{k} \cdot \boldsymbol{r}_j}. \tag{2.6}$$

CLS applies to cases where the scattering wavelength is very large compared to the mean free path and the detector response time is long compared to the molecule collision time. In the following experiments, the analysed wavelength will be of the order of 1 mm and the detecting system response time of the order of 10 ns. In these conditions, the discrete sum over molecular positions can be replaced by a number density integration on volume V. When the gas is a uniform mixture of different molecular species, the molecule polarization α_j can be replaced by the gas mean polarizability α.

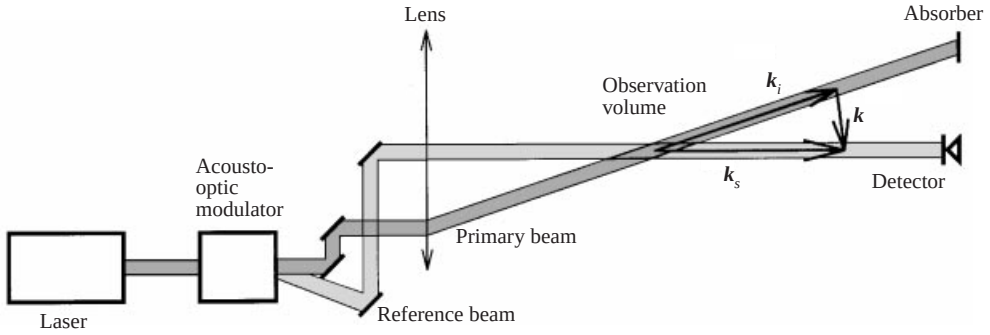

FIGURE 2. Heterodyne detection: a frequency shifted reference beam is created from the original laser beam by an acousto-optic modulator and sent to the detector. The interference term between the reference and the scattered beam is frequency shifted like the reference beam, and retains the phase and modulus information of the scattered beam. The beams crossing volume defines the observation zone.

The scattered electric field is then

$$\boldsymbol{E}_s(\boldsymbol{r}', t) = \frac{\pi\alpha}{N^2\lambda_i^2}\frac{\mathrm{e}^{\mathrm{i}k_s r'}}{r'}\mathrm{e}^{-\mathrm{i}\omega_i t}\boldsymbol{u}_s \wedge [\boldsymbol{u}_s \wedge \boldsymbol{E}_{io}] \int_V n(\boldsymbol{r}, t)\mathrm{e}^{-\mathrm{i}\boldsymbol{k}\cdot\boldsymbol{r}}\,\mathrm{d}^3\boldsymbol{r}. \tag{2.7}$$

In this equation, $\boldsymbol{E}_s$ is in the form of the product of the elementary scattered field from a single molecule located at the origin and the molecular density spatial Fourier transform along the scattering wavevector $\boldsymbol{k}$.

Rayleigh scattering uses the same molecular process, but it is performed in the 'non-coherent' regime, at very large wavevectors where the molecular mean free path smooths out the gas number density space distribution. CLS, however, is a 'coherent' Rayleigh scattering which only occurs when the number density is spatially non-uniform.

Turbulent gas flows, unlike quiescent gas flows, provide strong CLS signals. This will be commented upon later.

2.2. *Heterodyne detection*

Detectors responses are usually proportional to the received electromagnetic power. Plain detection of the scattered power would result in obtaining only the square of the complex field information (number density Fourier transform). In order to retain both the phase and modulus information of the Fourier transform, heterodyne detection is used. The optical layout is shown in figure 2.

Local oscillator

A reference beam (or 'local oscillator' beam) is created by an acousto-optic modulator, which shifts the laser light frequency by an harmonic HF frequency f_r (see figure 2). This reference beam is sent to the detector so as to interfere with the scattered light. The photo-electric current from the detector is then filtered to preserve only the interference term between the reference and the scattered electric field on the detector, at and around the HF frequency f_r. This interference signal is proportional to the scattered electric field amplitude (equation (2.7)) which modulates the monochromatic wave at the reference frequency f_r. Two further quadrature analog demodulation channels recover the complex amplitude of the scattered field.

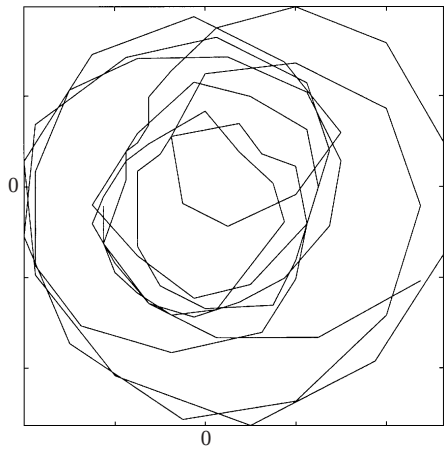

FIGURE 3. Typical CLS signal time evolution in the complex plane (real and imaginary parts are respectively horizontal and vertical axes). This signal is obtained from a supersonic mixing layer experiment. The scattering wavevector is along the flow. Axes units are arbitrary, but equal in both directions.

CLS signal

The two signals obtained from the two demodulation channels of the electronic device are respectively proportional to the real and imaginary parts of the number-density-space Fourier transform:

$$F_{\boldsymbol{k}}^{o}(t) = \int_{V} n(\boldsymbol{r}, t) \mathrm{e}^{\mathrm{i}\boldsymbol{k}\cdot\boldsymbol{r}} \, \mathrm{d}^3\boldsymbol{r}. \tag{2.8}$$

These signals are digitized in a time sequence and recorded for further computer treatment.

Signal modulus and phase

Figure 3 shows a typical CLS signal time evolution in the complex plane: horizontal and vertical axes are respectively the real and imaginary parts of the signal. Let us define the signal phase $\phi(t)$ and modulus $\rho(t)$ from

$$F_{\boldsymbol{k}}^{o}(t) = \int_{V} n(\boldsymbol{r}, t) \mathrm{e}^{\mathrm{i}\boldsymbol{k}\cdot\boldsymbol{r}} \, \mathrm{d}^3\boldsymbol{r} = \rho(t) \mathrm{e}^{\mathrm{i}\phi(t)}. \tag{2.9}$$

In figure 3, $\phi(t)$ and $\rho(t)$ are seen to have different roles and time behaviours. These will be explored in the next two sections.

3. Signal phase and velocimetry

Due to the Doppler effect the signal phase and frequency are linked to the flow velocity. This is further analysed and verified in a supersonic mixing layer experiment.

3.1. *CLS signal spectrum and velocimetry*

A direct connection between the CLS signal spectrum and the velocity probability distribution was first obtained by Grésillon & Cabrit (1991) and Grésillon *et al.* (1992).

CLS signal correlation

This connection is best analysed through the signal time correlation $C_F(\tau)$, which is defined as

$$C_F(\tau) = \langle F_{\boldsymbol{k}}^{o*}(t) F_{\boldsymbol{k}}^{o}(t+\tau) \rangle. \tag{3.1}$$

$F_{\boldsymbol{k}}^{o}(t)$ is written as a density volume integral (equation (2.8)):

$$C_F(\tau) = \left\langle \int_V n(\boldsymbol{r}, t) \mathrm{e}^{\mathrm{i}\boldsymbol{k}\cdot\boldsymbol{r}} \, \mathrm{d}^3\boldsymbol{r} \int_V n(\boldsymbol{r}', t+\tau) \mathrm{e}^{-\mathrm{i}\boldsymbol{k}\cdot\boldsymbol{r}'} \, \mathrm{d}^3\boldsymbol{r}' \right\rangle. \tag{3.2}$$

Fluid motion

The density volume integral at time $t+\tau$ can be replaced by a volume integral at time t. This is done by following the motion and distortion of each volume element $\mathrm{d}^3\boldsymbol{r}$ in $\boldsymbol{r}$ at time t during time τ: $\mathrm{d}^3\boldsymbol{r}'$ in $\boldsymbol{r}'$ at time $t+\tau$. This displacement is written as

$$\boldsymbol{\Delta}(\boldsymbol{r}, t, \tau) = \boldsymbol{r}(t+\tau) - \boldsymbol{r}(t). \tag{3.3}$$

According to particle conservation

$$n(\boldsymbol{r}', t+\tau) \, \mathrm{d}^3\boldsymbol{r}' = n(\boldsymbol{r}, t) \, \mathrm{d}^3\boldsymbol{r}. \tag{3.4}$$

The Fourier transform at time $t+\tau$ can be written as

$$\int_V n(\boldsymbol{r}', t+\tau) \mathrm{e}^{-\mathrm{i}\boldsymbol{k}\cdot\boldsymbol{r}'} \, \mathrm{d}^3\boldsymbol{r}' = \int_V n(\boldsymbol{r}'', t) \mathrm{e}^{-\mathrm{i}\boldsymbol{k}\cdot\boldsymbol{r}''} \mathrm{e}^{-\mathrm{i}\boldsymbol{k}\cdot\boldsymbol{\Delta}_{\boldsymbol{r}'',t,t+\tau}} \, \mathrm{d}^3\boldsymbol{r}'', \tag{3.5}$$

where $\boldsymbol{\Delta}_{\boldsymbol{r}'',t,t+\tau}$ is the flow displacement over time τ, of a fluid element located at $\boldsymbol{r}''$ at time t.

This equation is correct provided the integration volume which follows the fluid displacement has not significantly changed during a time τ_{C_F} characteristic of the molecular density correlation time. In this case, the correlation function can then be written as

$$C_F(\tau) = \left\langle \int_V n(\boldsymbol{r}, t) \mathrm{e}^{\mathrm{i}\boldsymbol{k}\cdot\boldsymbol{r}} \, \mathrm{d}^3\boldsymbol{r} \int_V n(\boldsymbol{r}'', t) \mathrm{e}^{-\mathrm{i}\boldsymbol{k}\cdot\boldsymbol{r}''} \mathrm{e}^{-\mathrm{i}\boldsymbol{k}\cdot\boldsymbol{\Delta}_{\boldsymbol{r}'',t,t+\tau}} \, \mathrm{d}^3\boldsymbol{r}'' \right\rangle. \tag{3.6}$$

For times shorter than signal correlation time τ_{C_F}, displacement is mostly due to the local volume mean velocity, $\bar{\boldsymbol{v}}_o$:

$$\boldsymbol{\Delta}_{\boldsymbol{r}'',t,t+\tau} = \bar{\boldsymbol{v}}_o \tau. \tag{3.7}$$

The signal correlation at short time is then only a function of density and mean velocity:

$$C_F(\tau) = \left\langle \left| \int_V n(\boldsymbol{r}, t) \mathrm{e}^{\mathrm{i}\boldsymbol{k}\cdot\boldsymbol{r}} \, \mathrm{d}^3\boldsymbol{r} \right|^2 \mathrm{e}^{-\mathrm{i}\boldsymbol{k}\cdot\bar{\boldsymbol{v}}_o\tau} \right\rangle. \tag{3.8}$$

Independence hypothesis

This analysis can be taken a step further since in most cases the square of the signal modulus $|\int_V n(\boldsymbol{r}, t) \mathrm{e}^{\mathrm{i}\boldsymbol{k}\cdot\boldsymbol{r}} \, \mathrm{d}^3\boldsymbol{r}|^2$ is not correlated with the phase term, $\mathrm{e}^{-\mathrm{i}\boldsymbol{k}\cdot\bar{\boldsymbol{v}}_o\tau}$.

This independence of velocity from density is the opposite of the strong Reynolds analogy (SRA), which links density and velocity fluctuations fields. But SRA is not appropriate, since in (3.8) density and velocity are taken at different scales and nonlinearly combined (density appears through a spatial Fourier transformation, and velocity as a spatial mean value inside a phase term).

We checked *a posteriori* that our data verified this assumption, by studying the

correlation: the correlation coefficient between CLS signal phase and modulus was found to be smaller than 10% in all cases.

Thus the signal correlation may be written as

$$C_F(\tau) = \left\langle \left| \int_V n(\boldsymbol{r}, t) \mathrm{e}^{\mathrm{i}\boldsymbol{k}\cdot\boldsymbol{r}} \, \mathrm{d}^3\boldsymbol{r} \right|^2 \right\rangle \left\langle \mathrm{e}^{-\mathrm{i}\boldsymbol{k}\cdot\bar{\boldsymbol{v}}_o\tau} \right\rangle . \tag{3.9}$$

The first factor does not depend upon τ. This can be written as the flow form factor $S(\boldsymbol{k})$:

$$S(\boldsymbol{k}) = \frac{1}{n_o V} \left\langle \left| \int_V n(\boldsymbol{r}, t) \mathrm{e}^{\mathrm{i}\boldsymbol{k}\cdot\boldsymbol{r}} \, \mathrm{d}^3\boldsymbol{r} \right|^2 \right\rangle . \tag{3.10}$$

The correlation time behaviour depends only on the second factor:

$$C_F(\tau) = n_o V S(\boldsymbol{k}) \left\langle \mathrm{e}^{-\mathrm{i}\boldsymbol{k}\cdot\bar{\boldsymbol{v}}_o\tau} \right\rangle . \tag{3.11}$$

Velocity distribution

The phase distribution is a statistical characteristic function. It can be written as

$$\left\langle \mathrm{e}^{-\mathrm{i}\boldsymbol{k}\cdot\bar{\boldsymbol{v}}_o\tau} \right\rangle = \int \mathrm{d}^3\bar{\boldsymbol{v}}_o \mathrm{e}^{-\mathrm{i}\boldsymbol{k}\cdot\bar{\boldsymbol{v}}_o\tau} P_{\bar{\boldsymbol{v}}_o}(\bar{\boldsymbol{v}}_o), \tag{3.12}$$

where $P_{\bar{\boldsymbol{v}}_o}$ is the volume mean velocity probability distribution.

From this expression, the CLS signal spectrum, $S_F(\omega)$, calculated as the correlation-time Fourier transform is

$$S_F(\omega) = \int C_F(\tau) \mathrm{e}^{\mathrm{i}\omega\tau} \, \mathrm{d}\tau = \pi n_o V S(\boldsymbol{k}) \int \mathrm{d}^3\bar{\boldsymbol{v}}_o \delta(\omega + \bar{\boldsymbol{v}}_o \cdot \boldsymbol{k}) P_{\bar{\boldsymbol{v}}_o}(\bar{\boldsymbol{v}}_o). \tag{3.13}$$

The signal frequency spectrum is seen as a projection of the velocity distribution along the scattering wavevector, $\boldsymbol{k}$:

$$S_F(\omega) \propto P_{\bar{v}_{o\parallel}}(v = -\omega/k) \tag{3.14}$$

where $P_{\bar{v}_{o\parallel}}$ is the one-dimensional velocity-probability-distribution, velocity component along the scattering wavevector axis:

$$P_{\bar{v}_{o\parallel}}(\bar{v}_{o\parallel}) = \int \mathrm{d}^2\boldsymbol{v}_\perp P_{\bar{\boldsymbol{v}}_o} \left(\bar{v}_{o\parallel} \frac{\boldsymbol{k}}{k} + \boldsymbol{v}_\perp \right) \tag{3.15}$$

and the signal frequency spectrum has the same form as the parallel velocity $\bar{v}_{o\parallel}$ distribution.

3.2. *Hydrodynamics modes*

The above analysis is restricted to cases where small-scale density fluctuations are convected at the mean flow velocity. This is a special case of fluctuations. It is interesting to relate it to a more general theory of fluid fluctuations.

It is known from a linear analysis of the inviscid fluid dynamics that three different orthogonal fluctuation modes can be simultaneously and independently excited. They are respectively the entropy, acoustic and vorticity modes (Chu & Kovásznay 1957). The entropy mode is a constant-pressure mode with associated density and temperature fluctuations convected by the flow: this is the mode that was assumed in the previous section. The acoustic waves also generate density fluctuations that are likely to be detected by CLS. At given scattering wavevector, the acoustic wave will be observed at a different frequency from that of the entropy mode since their propagation velocity is very different. The vorticity mode is only composed of velocity fluctuations with no associated density fluctuations. CLS cannot detect it directly.

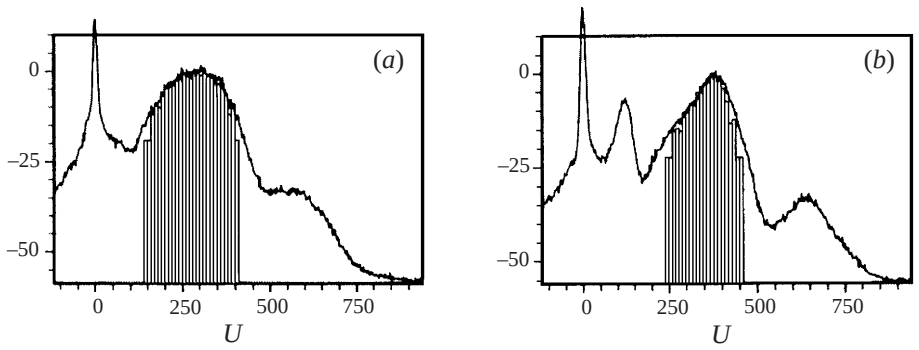

FIGURE 4. CLS signal spectrum (solid line) compared to laser Doppler velocimetry histograms, for two different positions inside a supersonic mixing layer: (*a*) corresponds to the centre of the mixing layer; (*b*) corresponds to a position which is closer to the faster flow. This figure is taken from Bonnet *et al.* (1995).

These properties are observed on experimental CLS spectra. This is shown in figure 4(*b*). There a typical CLS signal spectrum is shown as made up of three different peaks (excluding the instrumental nil velocity peak): the main peak, in the middle, corresponds to the entropy mode; it is centred on the characteristic Doppler convection frequency, equal to the mean flow velocity divided by the scattering wavelength: $f = \langle \bar{v}_{o\|} \rangle / \lambda$. On each side of this entropy peak, two other peaks are symmetrically situated. Their centre frequencies differ from the main peak frequency by the sound velocity, C, divided by the scattering wavelength: $f = (\langle \bar{v}_{o\|} \rangle \pm C)/\lambda$. These two peaks correspond to sound waves propagating in the fluid reference frame downwards and forwards, respectively.

3.3. *CLS spectrum and laser Doppler velocimetry*

The CLS signal frequency spectrum is made up of Doppler frequencies of the convected density inhomogeneities. It contains the same information as laser Doppler velocimetry (LDV). The noticeable difference is the nature of the scattering elements, but the way the Doppler effect links particle velocity to spectrum frequency is the same.

A comparison between CLS spectra and LDV has been made by Bonnet *et al.* (1995). The experiment was done in a wind tunnel where two atmospheric flows of different parallel velocities merged into a sheared-flow supersonic mixing layer. The CLS optics was aimed at different regions in the mixing layer situated at different positions in the transition region between the slower and the faster part of the flow. At each position, both the CLS signal spectrum and the LDV histogram were recorded. Figure 4(*a*, *b*) shows these two records obtained at two different positions inside the mixing layer. For comparison, the CLS spectrum horizontal frequency units have been converted into their Doppler velocity equivalents. Although the mean velocity is very different at these two positions, the agreement between the CLS spectrum and LDV histogram is good and conclusive evidence of the CLS spectrum accuracy.

3.4. *Signal phase and modulus: their relation to spectral analysis*

The complex signal phase and modulus have a different physical meaning and play a different role in the spectral analysis. The CLS complex signal $F_k(t)$ can be split into its modulus $\rho(t)$ and its exponential phase factor $e^{i\phi(t)}$.

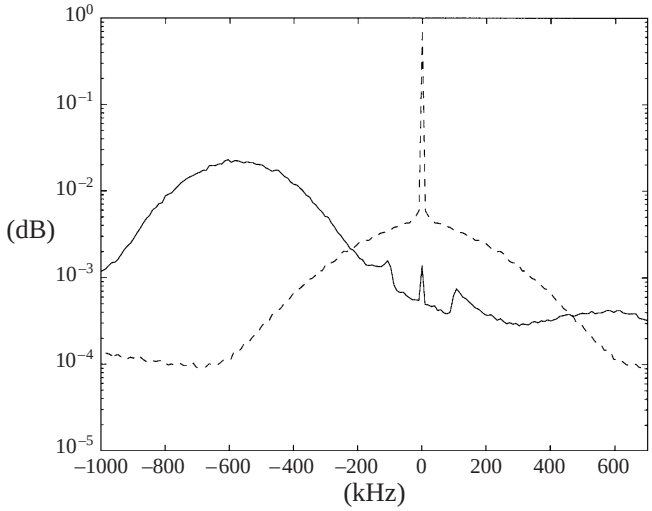

FIGURE 5. Phase exponential (solid line) and modulus (dashed line) spectra. Experiments are done in the centre of the mixing layer.

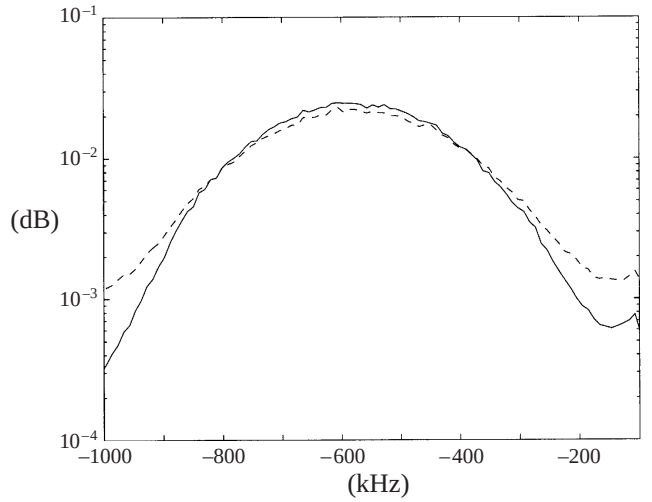

FIGURE 6. Phase exponential spectrum (dashed line), compared to the whole signal spectrum (solid line). Experiments are done in the centre of the mixing layer. Curves are normalized to their integral.

Figure 5 shows simultaneous frequency spectra of the modulus and of the phase factor, obtained in the supersonic mixing layer. We notice that the modulus spectrum is almost a delta function at null frequency. This is also seen when the mean-square modulus power $\langle\rho^2\rangle$ is compared to the squared mean modulus $\langle\rho\rangle^2$: we find that

$$\langle\rho\rangle^2 \sim 0.75\langle\rho^2\rangle. \tag{3.16}$$

This implies that the modulus can be supposed as roughly constant for the spectrum analysis:

$$\text{Spectrum}(\rho e^{i\phi}) \sim \langle\rho\rangle^2 \text{Spectrum}(e^{i\phi}). \tag{3.17}$$

This behaviour is confirmed in figure 6, which shows the signal frequency spectrum and the exponential factor frequency spectrum. Good agreement is obtained between

them. This is why the CLS signal phase can be assumed to contain mainly volume mean velocity information. Apart from the Doppler phase proportionality to the wavevector $\boldsymbol{k}$, this velocity information is the same whatever the observation scale k. Instead, the signal modulus carries information that is typical of a given scale. This is why the signal modulus will be explored from now on.

4. Form factor and the turbulent field structure at different spatial scales

Information about the scale of the scattering wavelength is obtained via the CLS signal modulus. This part of the signal can be used to probe the turbulence spatial spectrum since it provides direct information at a given scale. By optically tuning the wavenumber to different values, it is easy to sweep, in wavenumber space, the form factor (i.e. the signal modulus mean square) $\langle |F^o_{\boldsymbol{k}}(t)|^2 \rangle$.

As mentioned in Pao (1965*a*, *b*), density can be considered as a passive scalar field for the turbulence transport processes when turbulence is incompressible. For such a scalar field, Pao showed that the scaling law is the same as that of the kinetic energy. Thus we might expect a self-similar behaviour as seen from classical hot probes, except that our observation is in the wavevector three-dimensional space instead of the scalar frequency one-dimensional space. This is why the expected scale exponent is $|\boldsymbol{k}|^{-11/3}$ instead of $|\boldsymbol{k}|^{-5/3}$ since this latter is obtained from the former by a spherical integration over fluctuations of the same wavenumber spectrum,

$$\langle |F^o_{\boldsymbol{k}}(t)|^2 \rangle = \langle |n(\boldsymbol{k}, t)|^2 \rangle \propto k^{-11/3}. \tag{4.1}$$

A good choice of normalization for this quantity is that of the form factor,

$$S(\boldsymbol{k}) = \langle |n(\boldsymbol{k}, t)|^2 \rangle / \langle n \rangle V. \tag{4.2}$$

For a perfect gas at stationary thermodynamic equilibrium, the form factor is equal to unity whatever the value of $\boldsymbol{k}$. The CLS signal modulus mean-square absolute value for a given experiment can be obtained from proper signal calibration (Grésillon *et al.* 1982).

5. Air jet turbulence observed at two different scales

The inertial subrange is phenomenologically explained as resulting from a coupling, or a cascade, between different scales (Frisch 1995). Since CLS provides direct information at a given scale, it is interesting to observe simultaneously two CLS channels at a different scale and try to find their relation, if any.

5.1. *Biscattering device*

The initial CLS device is adapted to observe two independent scattering channels. This is shown in figure 7. The laser light is divided into three different beams by two acousto-optic modulators. Two of these beams, P1 and P2, are primary beams of equivalent power of about 1 W. The third one is the reference (LO) beam at a low power of a few mW. The light frequency is different for each of them.

The detector receives the reference electric field and the two scattered fields. The two beating terms, LO × P1 and LO × P2 are proportional to $F^o_{\boldsymbol{k}_1}(t)$ and $F^o_{\boldsymbol{k}_2}(t)$, with a different frequency shift (85 MHz and 40 MHz respectively). They are sorted using filters and recorded separately. Each of these signals is demodulated with a quadrature mixer and their real and imaginary parts are simultaneously digitized as in § 2.2.

Signals from each scattering are independent as long as the difference between

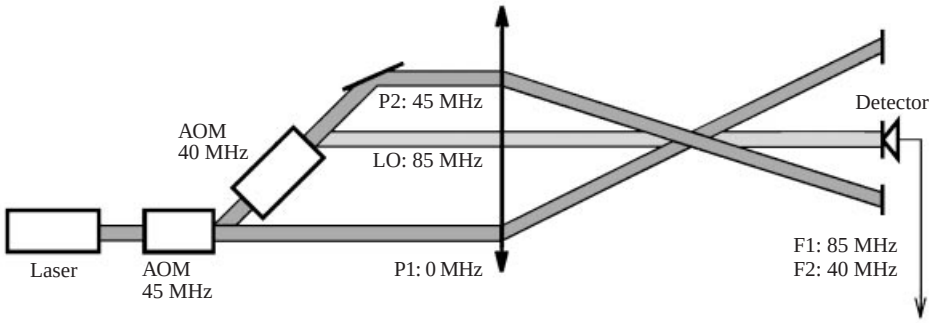

FIGURE 7. Double scattering observation device: Two incident beams (P1, P2) and one local oscillator (LO) are created from the laser beam, by acousto-optic modulators (AOM). The frequency differences allow to separate the two scattered signals in the detector current.

the scattering wavevectors, $\boldsymbol{k}_1 - \boldsymbol{k}_2$, is larger than the device wavenumber resolution Δk. Otherwise, a certain crosscorrelation is found between the signals. This crosscorrelation is proportional to the k volume overlap. For this device, the wavenumber resolution Δk is equal to $0.25\,\mathrm{mm}^{-1}$.

Technical parameters

The laser source is a CO_2 laser (wavelength: 10.6 μm). The scattering angle value is between $\theta = 8$ mrad and $\theta = 40$ mrad for both scattering channels. The resulting scattering wavelength is between 0.26 mm and 1.32 mm. The observation volume is a long cylinder of the same diameter as the incident beam diameter (12 mm), and a few decimetres long depending on the scattering angle.

The scattering signal is coming from that part of the volume where turbulence intensity is large enough. Since the turbulent field spatial extent is of the order of 1 cm long, it is much smaller than the length of the observed region and the turbulence region actually observed is a cylinder of 12 mm diameter and a few centimetres long, whatever scattering angle and collective scattering channels are used.

The signal modulation frequencies are 40 MHz and 85 MHz. The typical CLS signal frequency spectrum is contained in a frequency bandwidth of about 1 MHz. This is well within the detector bandwidth, which is larger than 100 MHz.

5.2. *Axisymmetric air jet turbulence*

The experiment was set-up to observe the air density fluctuations in an axisymmetric air jet (see figure 8). Clean compressed air is blown through a quieting honeycomb into a settling chamber, and then into the free atmosphere through a hole at the tip of a hollow drilled cone. The hole diameter is 1.5 mm. The generator pressure increment is between 0.5 and 1.5×10^5 Pa. This pressure is low enough to ensure a subsonic jet.

The observation volume is situated between 5 and 10 cm downstream of the jet nozzle. At these distances, the mean velocity on the axis is between 30 and $70\,\mathrm{m\,s}^{-1}$ and the turbulence is fully developed. For all the following experiments, the wavevectors are parallel to the streamwise direction.

For all these flows, the Reynolds number based on the nozzle diameter and the exit velocity, is more than 1.5×10^4. The exit velocity (around $300\,\mathrm{m\,s}^{-1}$) is estimated from the measured velocity at the downstream observation zone, and the phenomenological law of mean velocity variation along the symmetry axis. For an axisymmetric jet, the Reynolds number remains the same all along the axis (Hinze 1975).

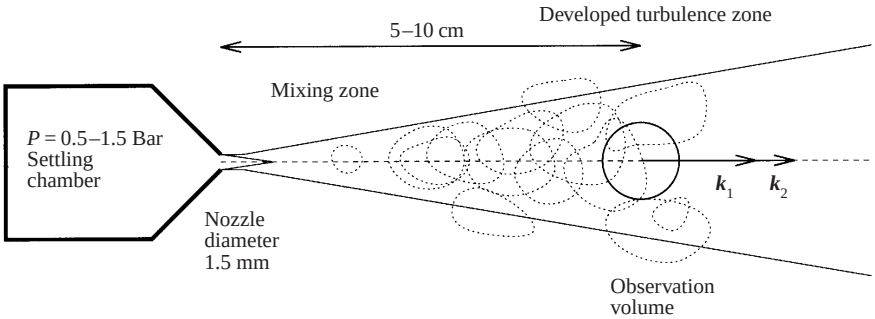

FIGURE 8. Axisymmetric air jet: the observation volume is a cylinder with a circular cross-section, crossing the jet axis a few centimetres from the nozzle. Both scattering wavevectors $\boldsymbol{k}$ are oriented in the streamwise direction.

6. Observation of turbulent field scale dynamics and coupling

The new information on the turbulent field provided by CLS will be divided into static and dynamic. Static data that is related to the well-known velocity field data is the form factor variation with spatial scale. The dynamical information from the CLS signal is the signal modulus (or the root form factor) time behaviour at given scale, and its correlation between different scales.

6.1. *Modulus mean values*

Form factor

The form factor variation with wavevector, proportional to the signal modulus mean square (cf. § 4) can be obtained from CLS observations at different wavenumbers in the jet turbulence field.

This is shown in figure 9, where the form factor is plotted as a function of wavenumber on log-log scales. To each factor is associated its error bar. One finds that the observed form factor is between 2×10^7 and 3×10^9. These values are very much larger than the thermodynamic value, which is unity. It decreases rapidly with k. A straight line can be plotted between these experimental values. The slope of this best linear fit is -3.5, close to the expected $k^{-11/3}$ Kolmogorov (three-dimensional) scaling law.

As a consequence of this fast decay, CLS signal analysis will benefit from a large signal to noise ratio at small wavenumber, and this signal to noise ratio will decay at larger ks.

Signal modulus variance

We observed that the CLS signal has the same statistical distribution of amplitude at different wavenumbers. More specifically the ratio between the variance and the mean square of the modulus does not depend on k.

Consequently, as a function of k, the mean modulus squared behaves in the same way as the modulus mean square (the form factor). The variance contains no specific information.

6.2. *Crosscorrelation function*

The previous results show that the Kolmogorov energy cascade scaling law also applies to the density fluctuations. In turn, the density fluctuation field could be used to probe more detailed cascade predictions.

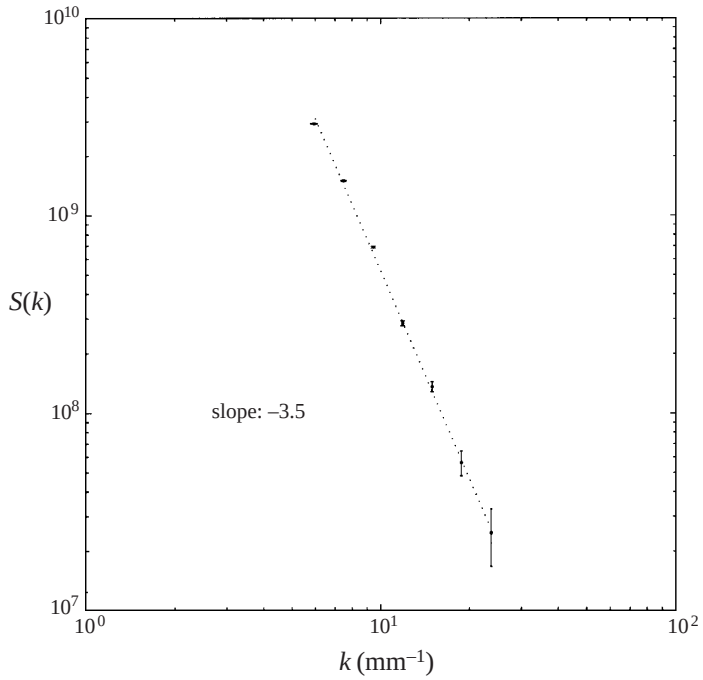

FIGURE 9. Form factor vs. wavenumber for developed jet turbulence. The generator pressure increment is 1.5×10^5 Pa. The observation zone is 50 mm downstream from the nozzle.

An interesting feature of CLS is that it gives temporal information for well defined wavenumbers. Using this information, it is interesting to check whether the cascade phenomenon leaves any signature on the temporal properties of CLS signal. Such an observation could also answer the question posed e.g. by Hinze (1975), "It would be interesting to establish experimentally whether in an actual turbulence the interaction between eddies is a local process in wavenumber space". For this purpose, we chose to correlate the CLS signal modulus at two different wavevectors k, for different times.

The signal modulus time crosscorrelation that we investigated is

$$C_{12}(\tau) = \langle |\tilde{\rho_{k1}}(t)||\tilde{\rho_{k2}}(t+\tau)| \rangle \tag{6.1}$$

where $\tilde{\rho}$ are is normalized CLS signal modulus fluctuations, defined as

$$\tilde{\rho_k}(t) = \frac{\rho_k(t) - \langle \rho_k(t) \rangle}{\langle |\rho_k(t) - \langle \rho_k(t) \rangle|^2 \rangle^{1/2}}. \tag{6.2}$$

6.3. *Typical crosscorrelation*

A typical CLS signal modulus time crosscorrelation function is shown in figure 10. This time correlation is obtained from two CLS signal channels observing air jet turbulence, on the axis of a 1.5 mm diameter round jet at a 0.5 bar source pressure, at a distance of 50 mm downstream. The two scattering wavevectors $\boldsymbol{k}_1$ and $\boldsymbol{k}_2$ are parallel to the mean flow and the analysing wavelengths are 0.33 and 0.66 mm respectively. Both signals were digitized simultaneously at a rate of 10 MHz, and a sample of 10^6 values were taken, this sequence being reproduced fifty times. In this way the statistical deviation of the normalized correlation was reduced to less than 10^{-3}.

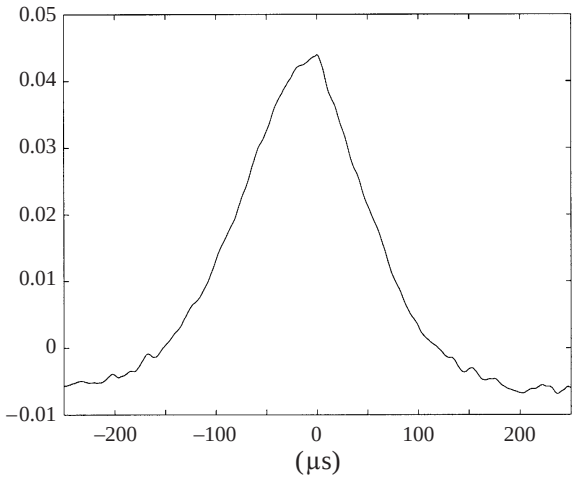

FIGURE 10. Typical CLS signal modulus crosscorrelation. The generator pressure increment is 0.5 bar. The observation zone is 50 mm downstream from the nozzle. Two CLS signals at scattering wavelengths 0.33 and 0.66 mm are crosscorrelated. This result was obtained from 50×10^6 samples recorded at a rate of 1 μs. The main part of the curve has a maximum crosscorrelation of 4.2 % near zero delay, and decays symmetrically in a time of the order of 70 μs (half-width at half-maximum).

Crosscorrelation level

A significant crosscorrelation between the two signals at different scales is observed. The correlation level is much larger than the statistical deviation: it is about 5% and in all experimental cases it is between 3% and 7%. The correlation rate is a little smaller when short lengthscales are observed, due to a smaller signal to noise ratio in each CLS channel.

Delay between scales

A remarkable feature of the time crosscorrelation function shown in figure 10 is that it is almost symmetrical. There are no signs of time asymmetry, no evidence that fluctuations at, say, the larger scale are leading fluctuations at the smaller scale. A significant coupling exists but there is no evidence that this coupling is time oriented. A slight negative time shift can however be observed in this figure, but it cannot be taken as significant since it may result from a spatial shift between the two observed CLS volumes. Indeed, the spatial position precision is estimated to be of the order of a millimetre; at a mean velocity of $50\,\mathrm{m\,s^{-1}}$ this is the distance travelled in 20 μs, which is of the order of the observed time shift.

The small additional correlation occurring over short times near to the time origin cannot be traced to a gas flow feature, since we found it to be a parasitic remanent of a cross-talk between channels. Both signals are coming from the same detector and pre-amplifier; although their heterodyne frequencies are very different, the slightest modulation in detector sensitivity or pre-amplifier gain results in a correlated signal at the same time. Small negative values at long times (above 120 μs) are remnants from a high-pass signal filtering at 2 kHz frequency.

The CLS channel wavevectors were changed in their specified range, and time crosscorrelation functions were formed for each pair. The same remarks always apply: the correlation function shows no significant time asymmetry. This is not the clear time delay one could have expected from a causal cascade from large scales to small scales. Information seems to circulate back and forth between scales.

λ_1 (mm)	λ_2 (mm)	$\bar{v}_o$ (m s^{-1})	L (mm)	τ_c (μs)
0.84	1.06	50	10	34
0.66				38
0.53				41
0.42				38
0.33				36
0.66	1.32	70	10	27
0.47	0.94			27
0.33	0.66			28

TABLE 1. Cross-correlation and scattering wavelength: values of measured cross-correlation timescale for each observed pair of wavelengths.

6.4. *Characteristic times and turbulence parameters*

In order to identify the characteristics of this crosscorrelation, the variation of the correlation with the main flow and scattering parameters have been investigated. Since the crosscorrelation function is a simple symmetric function with a maximum at the time origin, its experimental characteristic is the peak width τ_c. The correlation function is observed to be similar to a Gaussian. We determine the best Gaussian fit for the large-amplitude part where the correlation is larger than 20% of the maximum. The characteristic time τ_c is defined as the standard deviation of the fitted Gaussian distribution.

The four experimental free parameters are the generator pressure, the distance between nozzle and observation volume and both the scattering angles. These define the mean axial velocity, $\bar{v}_o$, the turbulent production lengthscale, L, and the scattering wavelengths, λ_1 and λ_2.

The mean velocity $\bar{v}_o$ is determined from the CLS signal spectrum, using its Doppler properties. It is obtained as the product of the mean frequency of the main spectrum peak times the scattering wavelength. The production lengthscale L is defined as the jet size at the observation zone. Because of the similarity properties of the jet, this scale is proportional to the distance from the nozzle (to within a few nozzle diameters) (Hinze 1975). We chose to define L as $L = z/5$ where z is the distance from the nozzle. Within this radial distance from the jet axis, the mean velocity at any position is at least 40% of the mean velocity on the axis.

Scattering wavelength

Two sets of experiments were done to study variation with the scattering lengthscales. The results are shown in figure 11. The parameters values are given in table 1. In the first series, shown in figure 11(*a*), one wavevector is kept constant and the other one is changed. Except for the longer wavelength case, the observed crosscorrelation function is maximum at the time origin with approximately constant peak width. The curve corresponding to the smallest wavelength difference shows a sharp peak of correlation at short timescale. This is because the difference between the two wavevectors is smaller than the device wavevector resolution (found to be equal to 0.25 mm^{-1}). Thus a part of both signals is common and results in a short time autocorrelation (cf. § 7). In the second series, shown in figure 11(*b*), the wavelength ratio is kept constant while both wavevectors are changed.

Comparing the two figures, the calculated characteristic times is seen to depend

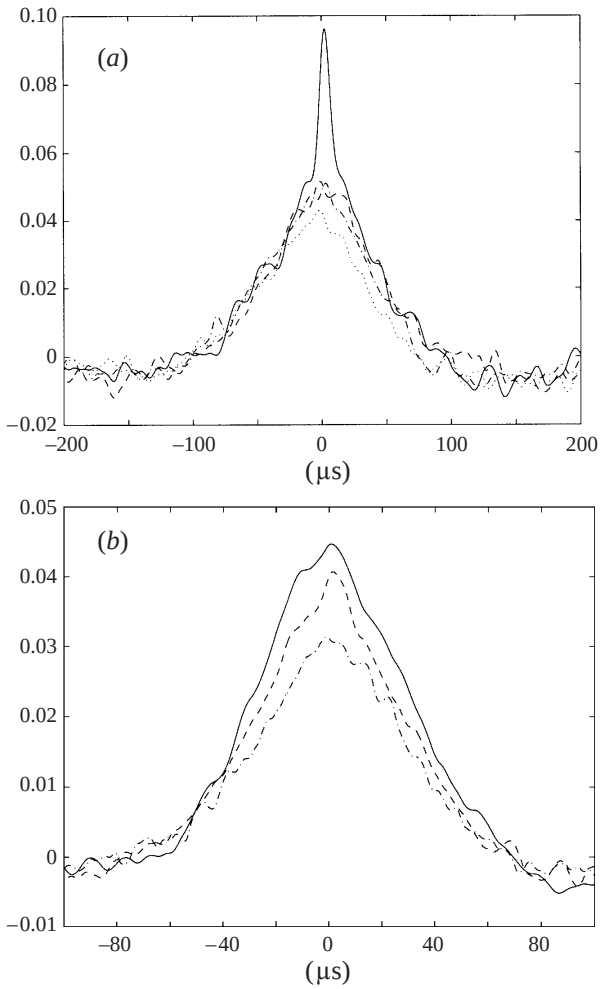

FIGURE 11. Crosscorrelation for different scattering scales: (*a*) experiments where one wavevector is kept constant while the other one is changed. The mean flow velocity is 50 m s^{-1}. The scattering wavelengths for each curve are: 0.84, 1.06 mm (solid); 0.66, 1.06 mm (dashed); 0.53, 1.06 mm (dash-dot line) and 0.42, 1.06 mm (dotted). (*b*) Experiments where the scattering scale ratio remains constant ($\frac{1}{2}$) while both scales are changed. The scattering wavelengths are: 0.66, 1.32 mm (solid line); 0.47, 0.94 mm (dashed line) and 0.33, 0.66 mm (dash-dotted line). The characteristic crosscorrelation time width can be seen to be nearly constant in every case.

on the mean velocity (decreasing for large $\bar{v}_o$), while it does not significantly depend upon the scattering lengthscale.

Mean axial velocity

The effect of the mean axial velocity was investigated by changing the jet generator pressure. The corresponding experimental parameters are given in table 2. The time crosscorrelation plots are shown in figure 12. As the velocity increases, the maximum correlation value does not change but the characteristic width is seen to decrease.

The crosscorrelation timescales are measured from figure 12. They are plotted on figure 13 as a function of velocity, in a log-log plot. The correlation time is seen to decrease when the velocity increases, almost linearly in this log-log plot. This suggests

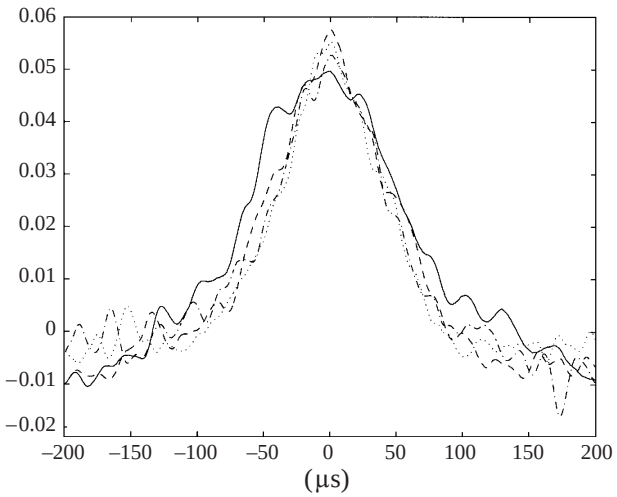

FIGURE 12. Crosscorrelation for different generator pressures. The mean velocity is changed by changing the generator pressure: 32 m s^{-1} (solid line), 37 m s^{-1} (dashed line), 43 m s^{-1} (dash-dot line) and 48 m s^{-1} (dotted line).

λ_1 (mm)	λ_2 (mm)	$\bar{v}_o$ (m s^{-1})	L (mm)	τ_c (μs)
0.66	1.32	32	10	47
		37		42
		43		39
		48		36
		51		33

TABLE 2. Crosscorrelation and mean axial velocity: values of measured crosscorrelation timescale for each mean axial velocity.

a power scale exponent can be found to relate the characteristic time variation with the velocity as

$$\tau_c \propto \bar{v}_o^{-0.8\pm0.3}. \tag{6.3}$$

This is very close to an inverse variation.

Turbulence production lengthscale

In a round free jet, the production lengthscale is known to be proportional to the distance between the observation volume and the jet nozzle. Changing this distance modifies not only the jet width in the observation volume, but also the mean velocity. The corresponding experimental parameters are given in table 3. The time crosscorrelation plots are shown in figure 14. The correlation time is seen to increase as the production length increases. The characteristic time width can be measured from this figure, and plotted as a function of the production scale. This is shown in figure 15, in log-log scale.

An approximate variation of τ_c as the square of L is observed. However these variations with L also include simultaneous variations of the velocity. These can be taken into account by using (6.3). When this is done, a parameter scaling law

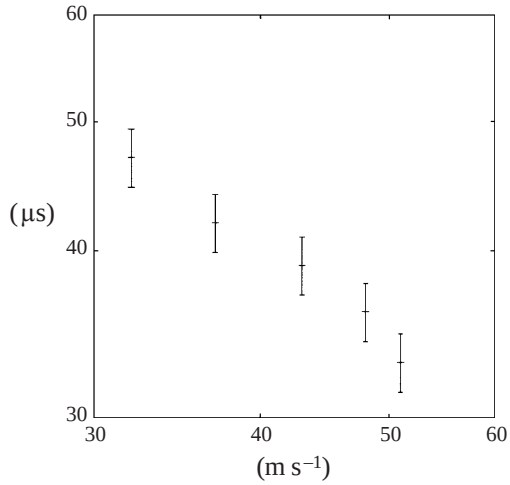

FIGURE 13. Cross-correlation timescale vs. mean axial velocity. The scales are logarithmic.

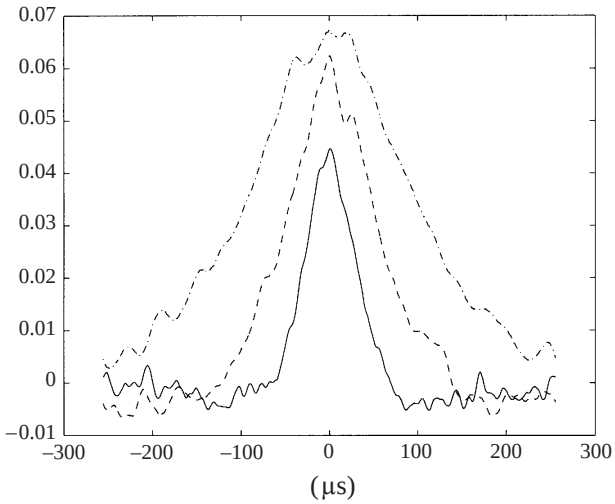

FIGURE 14. Crosscorrelation for different observation positions. The observed volume position along the jet axis is changed, accordingly changing the production length. The corresponding production lengthscales are: 10 mm (solid line), 14 mm (dashed line) and 20 mm (dash-dotted line). From one curve to the other, the mean velocity changes as it is inversely proportional to the production lengthscale.

including both velocity and production lengthscale can be obtained as

$$\tau_c \propto L^{1.0\pm0.3}\bar{v}_o^{-0.8\pm0.3}. \tag{6.4}$$

Large structures

The above result is compatible with a simple dimensional analysis by which the characteristic correlation time is

$$\tau_c \propto \frac{L}{\bar{v}_o}. \tag{6.5}$$

Thus the crosscorrelation time seems to correspond to the production time, i.e. to

λ_1 (mm)	λ_2 (mm)	$\bar{v}_o$ (m s^{-1})	L (mm)	τ_c (μs)
0.66	1.32	70	10	27
0.47	0.94			27
0.33	0.66			28
0.66	1.32	50	14	50
0.47	0.94			51
0.33	0.66			53
0.66	1.32	35	20	98
0.47	0.94			96
0.33	0.66			94

TABLE 3. Crosscorrelation and production lengthscale: values of measured crosscorrelation timescale for each production lengthscale.

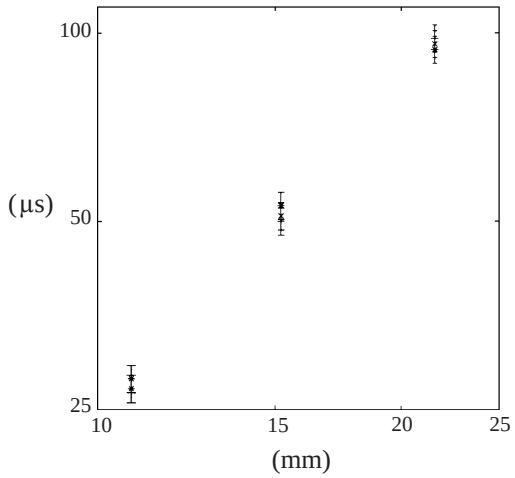

FIGURE 15. Crosscorrelation timescale vs. production lengthscale. The scales are logarithmic.

the characteristic lifetime of the largest turbulence structures that are convected at the mean velocity.

It should also be observed that the crosscorrelation level is the same whatever the different lengthscales. This implies that these turbulence structures drive simultaneously all the observed lengthscales. The turbulence intensity at large scale is simultaneously correlated with small-scale turbulence intensity.

Correlation and dust

Before concluding about characteristics that are intrinsic to turbulence, one should examine whether the observed crosscorrelation time could be due to dust particles blown through the observation scattering volume. Such particles would be simultaneously observed at any scale, giving rise to a significant correlation.

If this was the case, the experimental crosscorrelation time would be the time of flight of each particle inside the observation zone. This time of flight is of the same order as the observed correlation time. However it is also inversely proportional to the mean velocity and does not depend on the production lengthscale. This is not what is seen for the characteristic crosscorrelation time: it depends clearly on the production

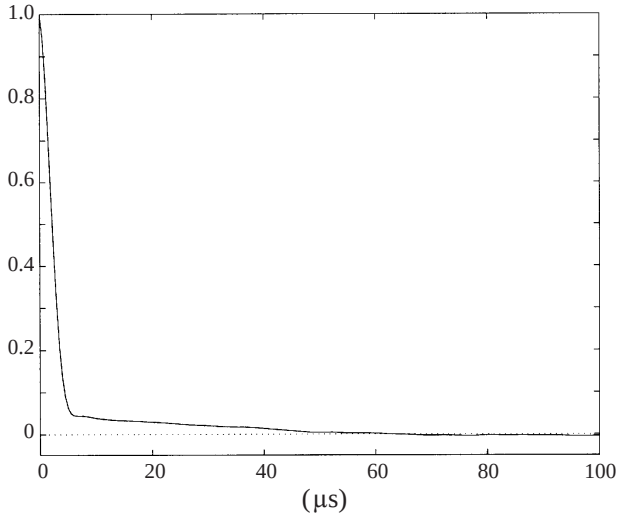

FIGURE 16. Typical CLS signal amplitude time autocorrelation. The generator pressure increment is 1.5×10^5 Pa. The position is 50 mm from the nozzle. The scattering wavelength is 0.66 mm. Two different timescales can clearly be observed: a short one of the order of a few microseconds, and a much larger timescale over which a small correlation is persistent.

timescale. Moreover the experimental crosscorrelation level does not depend on the scattering wavelength, while it should have in the presence of dust since the dust part of the signal should increasingly dominate over the turbulent part as the scattering wavelength becomes smaller.

We thus conclude that the characteristic time obtained from crosscorrelation between signals at different scales is not specific to the observed lengthscale, but is equal to the large turbulence structures lifetime.

7. Vortex turnover time and CLS time autocorrelation

The CLS signal amplitude time autocorrelation can be expected to provide more scale-specific information. This time autocorrelation function is

$$C_{11}(\tau) = \langle |\tilde{\rho_{k1}}(t)||\tilde{\rho_{k1}}(t+\tau)| \rangle \tag{7.1}$$

where use has been made of the normalized modulus fluctuations $\tilde{\rho_k}(t)$ defined in (6.2).

Typical autocorrelation

A typical signal autocorrelation function is shown in figure 16. As in figure 10, it was observed by recording the signal as 50×10^6 samples in successive sequences of 10^6 samples, at a rate of 10 MHz.

Two different timescales can clearly be seen on this figure. The autocorrelation first decreases from 1 to about 0.05 within a few microseconds. Then it decreases to 0 in a much longer period of a few tens of microseconds. This second part is very close to the previously shown crosscorrelation function: for the same (velocity and production scale) experimental conditions, these correlation levels and timescales are identical. The same large-lengthscale phenomena are most likely responsible for this behaviour.

The short autocorrelation timescale τ_s is worth investigating. It will be quantitatively

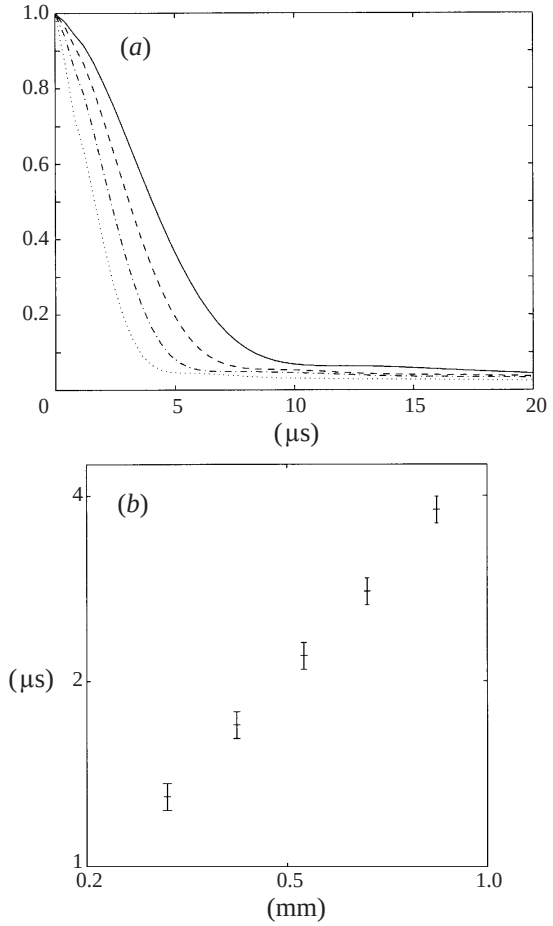

FIGURE 17. Autocorrelation and scattering wavelength: (*a*) the time autocorrelations. The observation position is 50 mm from the nozzle. The mean flow velocity is 50 m s^{-1}. The wavelength for each curve is: 0.84 mm (solid line), 0.67 mm (dashed line), 0.53 mm (dash-dotted line) and 0.42 mm (dotted). (*b*) The short timescale vs. the scattering lengthscale. The scales are logarithmic.

defined as the standard deviation of that part of the time correlation function with amplitude larger than 0.05, treated as a distribution. As previously, we study how it varies when the main experimental free parameters are modified: jet pressure increment, observation position from the nozzle and scattering wavelength.

Scattering wavelength

Figure 17 shows autocorrelation functions obtained for different scattering wavelengths (*a*), and the corresponding characteristic times as a function of this scattering wavelength (*b*). The observation position is 50 mm from the nozzle. The mean flow velocity is 50 m s^{-1}. The results for the short timescale τ_s are reported in table 4. The autocorrelation time width is seen to increase with wavelength.

A scaling law can be found from these results:

$$\tau_s \propto \lambda^{+1.15\pm0.2}. \tag{7.2}$$

λ (mm)	$\bar{v}_o$ (m s^{-1})	L (mm)	τ_s (μs)
0.33	50	10	1.3
0.42			1.7
0.53			2.2
0.67			2.8
0.84			3.8

TABLE 4. Autocorrelation and scattering wavelength: values of measured short timescale for each scattering wavelength.

λ (mm)	P (10^5 Pa)	$\bar{v}_o$ (m s^{-1})	L (mm)	τ_s (μs)	λ (mm)	$\bar{v}_o$ (m s^{-1})	L (mm)	τ_s (μs)
0.66	0.5	32	10	4.3	0.66	70	10	2.0
	0.7	37		3.4	0.47			1.4
	0.9	43		3.0	0.33			0.98
	1.1	48		2.8				
	1.3	51		2.5	0.66	50	14	3.3
					0.47			2.2
					0.33			1.65
					0.66	35	20	5.7
					0.47			3.8
					0.33			2.7

TABLE 5. Autocorrelation timescale variation with mean velocity and production lengthscale. These parameters were modified by changing the observation position or the jet pressure.

Mean velocity and production lengthscale

Table 5 shows the variations of the autocorrelation short timescale when the jet generator pressure varies from 0.5 to 1.3×10^5 Pa and when the observation position from the jet varies from 50 mm to 100 mm. From these results, the characteristic autocorrelation timescaling law with mean velocity and production lengthscale (figure 18) can be obtained as

$$\tau_s \propto L^{0.4\pm0.3}\bar{v}_o^{-1.15\pm0.3}. \tag{7.3}$$

Observed structures

From the previous two observations, the characteristic autocorrelation short timescaling law τ_s is

$$\tau_s \propto \lambda^{+1.15\pm0.2}L^{+0.4\pm0.3}\bar{v}_o^{-1.15\pm0.3}. \tag{7.4}$$

This law can be made similar to the eddy turnover timescaling law, present in the Kolmogorov theory:

$$\tau_{turnover} \propto \lambda^{2/3}L^{1/3}\bar{v}_o^{-1}. \tag{7.5}$$

The observed variations with production scale and mean velocity are close to this value. However, the experimental variation with the wavelength λ is stronger. Since the experimental law for τ_s does not have the right dimension, the τ_s variations must depend on another parameter. The eddy turnover phenomenon seems not to be the only effect; there may be some contribution due to e.g. the finite observation volume.

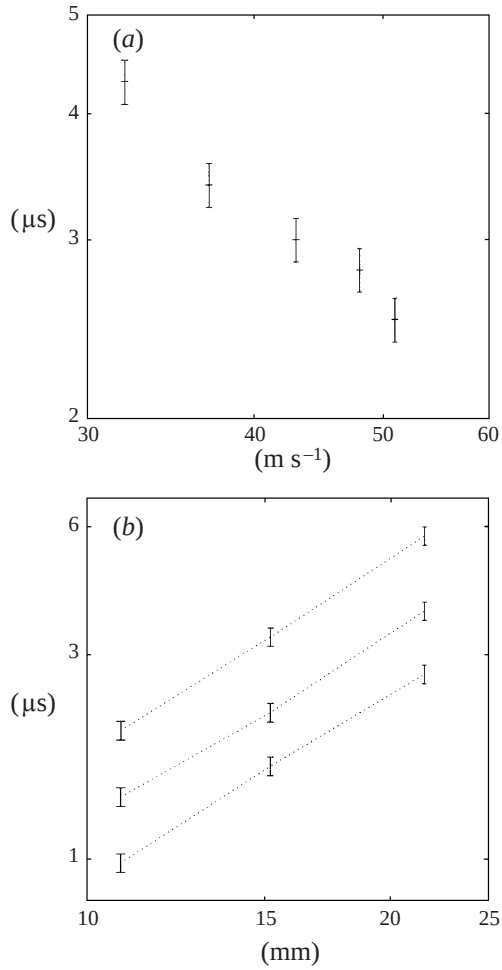

FIGURE 18. Autocorrelation timescale variation with main turbulence parameters: timescale scaling law with mean velocity (*a*) and production lengthscale (*b*).

8. Conclusion

With the help of collective light scattering, experimental investigations of a fully developed turbulent field have been made with direct observations of the space Fourier transforms at given spatial scales. The time behaviours of different scales and their correlation have been obtained. With regard to the cascade phenomenology, it is found that eddy turnover timescaling law is close to the law for the autocorrelation characteristic time. Moreover, the crosscorrelation level between any two different scales is significant. But the experimental crosscorrelation time shows three main differences with the cascade model: the characteristic time is much longer than eddy turnover time, it does not depend on the scale size ratio, and it does not show any significant time asymmetry. Perhaps not surprisingly, the crosscorrelation time is found to be the turbulence production time. We think these findings can be useful for building pertinent phenomenological turbulence models.

This work has been supported by grant number 94-112 from 'Direction des Recherches et Études Techniques' of the French ministry of defense.

REFERENCES

Benedek, G. 1964 Optical mixing spectroscopy, with application to problems in physics, chemistry and engineering. In *Polarisation, Matière et Rayonnement* (ed. S. F. Phys), pp. 49–84. Paris: PUF.

Bonnet, J., Grésillon, D., Cabrit, B. & Frolov, V. 1995 Collective light scattering: a non particle laser velocimetry. *Meas. Sci. Technol.* **6**, 620–636.

Chu, B. & Kovásznay, L. 1957 Non-linear interactions in a viscous heat-conducting compressible gas. *J. Fluid Mech.* **3**, 494–514.

Cummins, H., Knable, N. & Yeh, Y. 1964 Observation of diffusion broadening of Rayleigh scattered light. *Phys. Rev. Lett.* **12**, 150–153.

Cummins, H. & Swinney, H. 1970 Light beating spectroscopy. In *Progress in Optics VIII* (ed. E. Wolf), pp. 135–196. North-Holland.

Frisch, H. 1967 Study of turbulence by spectral fine structure of scattered light. *Phys. Rev. Lett.* **19**, 1278–1279.

Frisch, U. 1995 *Turbulence: The Legacy of A.N. Kolmogorov*. Cambridge University Press.

Gennes, P. G. de 1966 L'observation des corrélations de vitesse et de pression dans un écoulement turbulent. *C. R. Acad. Sci. Paris* **262**, 74–77.

Grésillon, D. & Cabrit, B. 1991 Collective scattering and fluid velocity fluctuations. In *A Variety of Plasmas: Proc. Intl Conf. on Plasma Physics, New Delhi 1989* (ed. A. Sen & P. Kaw), pp. 173–187. India: Pramana Bengalore.

Grésillon, D., Cabrit, B. & Iwana, N. 1993 Nonlinear analysis signal in a fluid turbulence: a comparison between bispectrum and mutual information. *Conference on Wave Phenomena in Solar-Terrestrial Plasmas, Oslo*.

Grésillon, D., Cabrit, B., Villain, J., Hanuise, C., Truc, A., Laviron, C., Hennequin, P., Gervais, F., Quémeneur, A., Garbet, X., Payan, J. & Devynck, P. 1992 Collective scattering of electromagnetic waves and crossed-B plasma diffusion. *Plasma Phys. Controlled Fusion* **34**, 1985–1991.

Grésillon, D. & Mohamed-Benkadda, M. S. 1988 Direct mode-mode coupling observation in the fluctuations of nonstationary transparent fluid. *Phys Fluids* **31**, 1904–1909.

Grésillon, D., Stern, C., Hémon, A., Truc, A., Lehner, T., Olivain, J., Quémeneur, A., Gervais, F. & Lapierre, Y. 1982 Density fluctuations measurement by far infrared light scattering. *Physica Scripta* **T2/2**, 459–466.

Hinze, J. 1975 *Turbulence*, 2nd edn. McGraw Hill.

Holzhauer, E. & Massig, J. 1978 An analysis of optical mixing in plasma scattering experiments. *Plasma Phys.* **20**, 867–877.

Jackson, J. 1975 *Classical Electrodynamics*, 2nd edn. J. Wiley & Sons.

Lelièvre, J. & Picard, J. 1980 Observation d'une lumière laser diffusèe par un gaz en mouvement turbulent. *C. R. Acad. Sci. Paris* **290**, 473–476.

Orszag, S. 1977 Lectures on the statistical theory of turbulence. In *Fluid Dynamics* (ed. R. Balian & J.-L. Peube) les Houches, 1973. Gordon & Breach.

Pao, Y. 1965*a* Structure of turbulent velocity and scalar fields at large wavenumbers. *Phys. Fluids* **8**, 1063–1075.

Pao, Y. 1965*b* Transfer of turbulent energy and scalar quantities at large wavenumbers. *Phys. Fluids* **11**, 1371–1372.

Stern, C. & Grésillon, D. 1983 Fluctuations de densité dans la turbulence d'un jet. Observation par diffusion rayleigh et détection hétérodyne. *J. Phys. Paris* **44**, 1325–1335.

Yeh, Y. & Cummins, H. 1964 Localized fluid flow measurements with an He-Ne laser spectrometer. *Appl. Phys. Lett.* **4**, 176–178.